Article

Tuning the Chemical and Electrochemical Properties of Paper-Based Carbon Electrodes by Pyrolysis of Polydopamine

Jaqueline F. Rocha, Julia C. de Oliveira, Jefferson Bettini, Mathias Strauss, Guilherme S. Selmi, Anderson K. Okazaki, Rafael F. de Oliveira, Renato S. Lima, and Murilo Santhiago*

Cite This: https://doi.org/10.1021/acsmeasuresciau.3c00063

Read Online

ACCESS | Metrics & More | Article Recommendations | SI Supporting Information

ABSTRACT: Electrochemical paper-based analytical devices represent an important platform for portable, low-cost, affordable, and decentralized diagnostics. For this kind of application, chemical functionalization plays a pivotal role to ensure high clinical performance by tuning surface properties and the area of electrodes. However, controlling different surface properties of electrodes by using a single functionalization route is still challenging. In this work, we attempted to tune the wettability, chemical composition, and electroactive area of carbon-paper-based devices by thermally treating polydopamine (PDA) at different temperatures. PDA films were deposited onto pyrolyzed paper (PP) electrodes and thermally treated in the range of 300−1000 °C. After deposition of PDA, the surface is rich in nitrogen and oxygen, it is superhydrophilic, and it has a high electroactive area. As the temperature increases, the surface becomes hydrophobic, and the electroactive area decreases. The surface modifications were followed by Raman, X-ray photoelectron microscopy (XPS), laser scanning confocal microscopy (LSCM), contact angle, scanning electron microscopy (SEM-EDS), electrical measurements, transmission electron microscopy (TEM), and electrochemical experiments. In addition, the chemical composition of nitrogen species can be tuned on the surface. As a proof of concept, we employed PDA-treated surfaces to anchor $[AuCl_4]^-$ ions. After electrochemical reduction, we observed that it is possible to control the size of the nanoparticles on the surface. Our route opens a new avenue to add versatility to electrochemical interfaces in the field of paper-based electrochemical biosensors.

KEYWORDS: pyrolyzed paper, polydopamine, gold nanoparticles, chemical functionalization, electrochemical devices
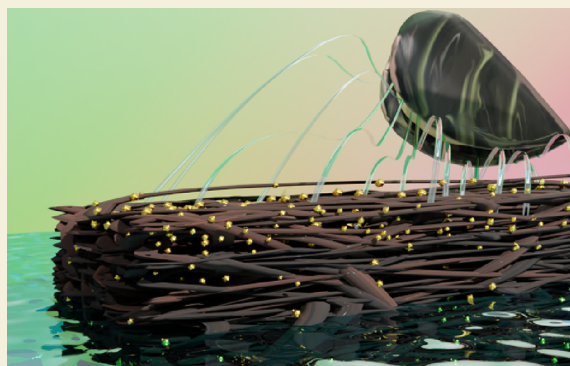
1. INTRODUCTION

Electrochemical paper-based analytical devices (ePADs) have gained a lot of interest in many areas since 2009 when the first patterning routes for electrode fabrication were described on paper substrates.[1,2] Such devices can be compact, flexible, easy-to-use, and affordable and have been successfully demonstrated for the preparation of electrochemical biosensors,[3] sensors,[4−6] supercapacitors,[7] and batteries.[8] In addition, the porosity of paper is a key advantage when compared to conventional subtrates, allowing a capillary flow of supporting electrolytes[9] or precursors[4,10,11] for the fabrication of three-dimensional circuits and electrochemical cells on paper. Among the many materials available for electrode fabrication, carbon is a remarkable example due to its low cost, high chemical stability, high electrical conductivity, and large availability. In addition, carbon present itself in many different forms like carbon black,[12,13] carbon nanotubes,[14] fullerene,[15] graphene and derived forms,[16,17] and graphite,[18,19] giving rise to many

possibilities to select the proper carbon-based material for the final application.

Most of carbon-based electrodes are prepared on paper using conductive inks combined with patterning routes such as screen-printing[20] and inkjet printing.[6] These routes have been pushing the field with remarkable applications in the last years.[21,22] In terms of the carbon source, there is an increasing interest in obtaining high-conductive carbon micronanoparticles using sustainable precursors. For example, lignocellulosic biomass can be converted into conductive particles by pyrolysis at high temperatures[23,24] and used for the preparation of conductive tracks on paper.[25] Lignocellulosic materials

contribute as a source of carbon, while pyrolysis converts the carbons from sp^3 to sp^2 hybridization. Another possibility is to directly pyrolyze substrates that are based on cellulose for the fabrication of electrical and/or electrochemical devices.[26] This process can be performed by using two main routes. First, photothermal pyrolysis performed using laser engraving systems, e.g. CO_2, locally converts cellulose into highly conductive carbon-based material. The process is fast and enables the patterning of conductive tracks on a variety of lignocellulosic substrates.[27] The second alternative relies on the use of a tubular furnace in a controlled inert atmosphere that converts the entire cellulosic material into carbon. Such route allows the control of the temperature during the process and several sheets of cellulose can be pyrolyzed in a single run.[28−31] The resulting material is hydrophobic since most of the oxygen-rich chemical groups are lost after pyrolysis. Thus, to tune the surface properties of paper-based carbon electrodes, a further functionalization step is mandatory.

In 2007, inspired by the facility of mussels to adhere in all kinds of surfaces in water, Messersmith et al. described a very interesting route for the fast preparation of simple, biocompatible, and versatile coatings on many different types of surfaces.[32] The polymerization occurs in a buffered solution in the presence of dopamine resulting in the formation of PDA coatings on all objects immersed, independent of their surface chemistry.[33,34] Thus, PDA formation adds nitrogen and oxygenated groups to the interface and converts hydrophobic surfaces into hydrophilic.[34−36] These remarkable features have been explored in the field of electrochemical sensors through the functionalization of carbon electrodes.[18,28,37,38] PDA-functionalized carbon electrodes have been designed to detect organic molecules,[39] biomarkers,[40] and viruses.[41] In addition, the combination of PDA with 2D materials,[40] conductive polymers,[42] and nanoparticles[43] has been demonstrated to improve the sensitivity of electrochemical sensors and biosensors. However, it is still very challenging to tune multiple surface properties of PDA without adding additional chemical reagents. Thus, inspired by the chemical changes that occur in cellulose after pyrolysis, e.g., loss of chemical groups, we attempt to tune the surface properties of electrodes modified with PDA by performing pyrolysis steps at different temperatures. This feature is particularly important to allow capillary-driven aqueous solutions in hydrophobic and porous pyrolyzed carbon electrodes. By controlling the flow-through in these electrodes it is possible to tune the area of electrodes,[30,44] filtrate samples, and fabricate three-dimensional (3D) devices by stacking multiple sheets of paper.[45] These features were recently studied by dropping isopropanol[44] or surfactants[30] before the analysis and by using O_2 plasma to allow capillary-driven of aqueous solutions.[45] Although interesting, these strategies present limited wettability or require a hydrophilic material to assist the capillary flow. Thus, PDA has the potential to meet such challenges and expand interfacial features of porous carbon electrodes by exploring nitrogen-based surface chemistry. To the best of our knowledge, pristine and carbonized PDA were not systematically studied to tune many surface properties of porous electrode materials. In particular, the control of size, distribution, and distribution of gold nanoparticles (AuNPs) along the thickness of the electrodes due to the surface chemistry of pyrolyzed fibers was not reported so far.[34,46]

In this work, we reported for the first time the tuning of wettability, surface chemistry, coating thickness, and area of the electrodes by pyrolysis of PDA on PP. First, we obtained PP electrodes using a route described in the literature.[29,43−45] Next, PP electrodes were incubated in the presence of dopamine at pH 8.5 until complete evaporation of the solvent resulting in the formation of PDA film of approximately 3.0 μm. The presence of PDA was confirmed by spectroscopy analysis. Thermally treated PDA up to 1000 °C showed surface transitions from superhydrophilic to hydrophobic and thickness reduction from micro to nanometer, and tunable N-based groups were observed. The abundance of nitrogen is reduced as the temperature increases. However, we confirmed the presence of the N-based group in all temperatures by performing spectroscopic analyses of the surfaces. Electrochemical experiments also revealed that the area of the electrodes can be tuned, and the charge transfer resistance (R_{ct}) decreased. Finally, as a proof of concept, we explored the tunable surface chemistry of the electrodes to prepare AuNPs. The size, concentration, and position (volume or outer face) of AuNPs can be changed by the appropriate temperature in the pyrolysis process.

2. MATERIALS AND METHODS

2.1. Paper Pyrolysis and PDA Functionalization

Whatman #1 chromatographic paper was pyrolyzed in a tubular furnace (Lindberg/Blue M from Thermo Fisher Scientific, USA). First, strips of paper (10.0 × 2.5 cm) were cut and placed between alumina plates to avoid wrinkles after thermal treatment. After placing the substrates inside the tube, a purging step with nitrogen gas (N_2) (99.99%) was conducted at 5 L min^{-1} for 5 min to remove oxygen from the alumina tube. The furnace was heated from 25 to 1000 °C at a rate of 20 °C min^{-1}. The furnace was kept at 1000 °C for 1h and then it was allowed to cool at room temperature. During the pyrolysis process, we kept N_2 at a flow rate of 20 L min^{-1} flowing through the tube to remove gases produced.

PP strips were functionalized with PDA using the chemical route[32] reported. Dopamine hydrochloride (Sigma-Aldrich) was dissolved in 10 mM Tris buffer (Sigma-Aldrich) pH 8.5 to prepare a solution of 2 mg mL^{-1}. PP strips were immersed in this solution for 24 h in a closed bath to minimize evaporation of the solution. After, the lid was removed, and the solution was allowed to dry in the reservoir. After the functionalization of PP with PDA (PP + PDA), we performed a second stage of pyrolysis at different final temperatures of 300, 400, 500, 700, and 1000 °C using the same heating rate in all cases.

2.2. Electrochemical Experiments and Au Nanoparticle Functionalization

Electrochemical measurements were done using an AutoLab potentiostat, model PGSTAT302N, from Eco Chemie, Netherlands. We employed a three-electrode system with Ag/AgCl (3.0 mol L^{-1} KCl, Metrohm), glassy carbon plate (SynLectro) and PP as reference (RE), counter-electrode (CE), and working electrode (WE), respectively. To fabricate the WE, 1 × 1 cm square sheets of PP were cut and attached to a glass slide by using double-sided tape. Next, electrical contact tracks were patterned using silver ink (SPI Supplies, USA). The active area of WE was isolated by attaching an adhesive layer containing a hole (d = 2.0 mm) on PP. Finally, we attached a second adhesive layer to isolate the silver layers, as schematically shown in Figure S1. Cyclic voltammograms were obtained in the presence of the redox probe 5.0 mM $[Fe(CN)_6]^{3-/4-}$ or $[Ru(NH_3)_6]Cl_3$ (Sigma-Aldrich) in KCl 0.5 M (Merck) as the supporting electrolyte at 30 mV s^{-1}. For the scan rate tests, the variation was from 10 to 300 mV s^{-1}. The electrochemical impedance spectroscopy (EIS) experiments were conducted by applying the open-circuit dc potential, 10.0 mV ac voltage, 2 s integration time, and frequencies from 1 to 10^5 Hz at room temperature.

For the functionalization with gold using PP and PDA-modified samples, the electrodes were incubated in a 5 mM $HAuCl_4$ (Sigma-
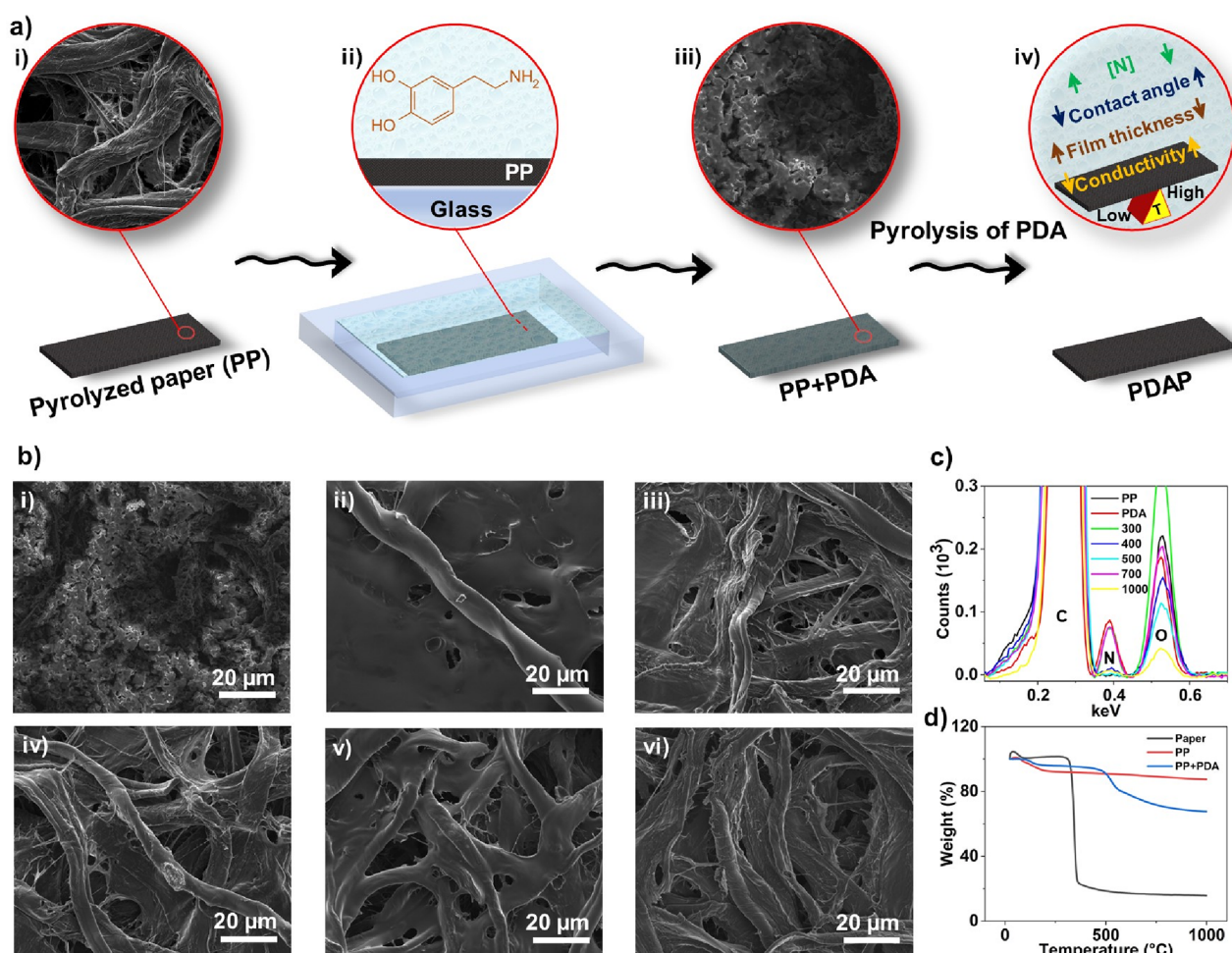
Figure 1. (a) Schematic illustration of the functionalization and pyrolysis process. (b) SEM images of PP modified with PDA at different temperatures (°C) for (i) 25, (ii) 300, (iii) 400, (iv) 500, (v) 700, and vi) 1000. (c) Single-point EDX spectra. (d) Thermogravimetric curve for paper, PP, and PDA-coated PP.

Aldrich) solution for 30 min and then washed with deionized water. Next, adsorbed $[AuCl_4]^-$ ions were electrochemically reduced by scanning the potential at 30 mV s^{-1} in the rage of 0.0 to −1.3 V vs Ag/AgCl electrode in 0.1 M acetate buffer (Sigma-Aldrich) at pH 4.0.

2.3. Characterization

Electrical measurements were performed by placing a sheet of the pyrolyzed sample between two glass slides. The bottom glass slide contains patterned gold conductive tracks, as schematically shown in Figure S2. Electrical resistance was measured by placing the probes on the gold conductive pads using a Minipa multimeter, model ET-2082C. Resistivity values (ρ) were obtained from the slopes of resistance (R) versus distance graphs. An Attension TheTa L tensiometer with readings in the OneAttension software was used to measure the static contact angle of the samples. Thermogravimetric analyses were run using a Jupter Netzsch equipment model STA F3. To evaluate the mass loss, the samples were heated from 25 to 1000 °C using a heating rate of 20 K min^1. For morphological analysis of the material, scanning electron microscopy (SEM) images were taken at 5 kV operating voltage using the Thermo Fisher Scientific microscope, model Inspect F50 with an energy dispersive X-ray spectrometer (EDS) from Oxford System. Assisted pyrolysis was performed by SEM *in situ* heating stage, as shown in Figure S3, using the HT-GSED detector, energy 20 kV, heating rate 18 °C min^{-1} (from 50 to 600 °C images were taken at an increasing rate of 50 °C, then from 600 to 1000 °C at 100 °C and pressure of 120 Pa). X-ray photoelectron spectroscopy (XPS) from Thermo Scientific containing a monochromatic microfocused Kα source with a resolution of 0.100 eV, energy transfer of 50 eV, spot size of 300 μm, and 10 scans

was used to study the surface chemistry of the samples. A laser scanning confocal microscope (LSCM) from Keyence, model VK-X200, was used to obtain the roughness of the electrodes in large areas. PDA film thicknesses were obtained by atomic force microscopy (AFM) using equipment from Park Systems, model NX10. The measurements were done using a FMR probe (Nano-World) with a nominal spring constant of 2.8 N/m, 10.0 nm tip end radius, and resonance frequency of 75 kHz. Si substrates were partially coated using AZ5214 photoresist, and after PDA formation, the sample was washed with acetone. The PDA adhered on Si was pyrolyzed, and the thickness of PDA was measured using AFM. Raman spectra were obtained with equipment from Renishaw, model Via Micro-Raman, with a 633 nm laser and power of 50% to determine the degree of graphitization of the PP. Data were treated with the software FityK.

Transmission electron microscopy (TEM) and scanning transmission electron microscopy (STEM) were used to analyze the PDA layer on the top of PP and PDA isolated before and after the heating process. TEM and STEM images were acquired using a microscope with a Field Emission Gun source and operating a 200 kV voltage. Thickness and morphology of the PDA layer on the top of PP before and after the heating process were analyzed using TEM and STEM images. Compositional maps of the interface were obtained by energy electron loss spectroscopy (EELS). The samples for these analyses were prepared by an ultramicrotomy process; the samples were embedded in an Eponate 12 resin with benzyldimethylamine. This resin was infiltrated with propylene oxide for 1 h at different concentrations. Finally, the samples were cut using a Pelco
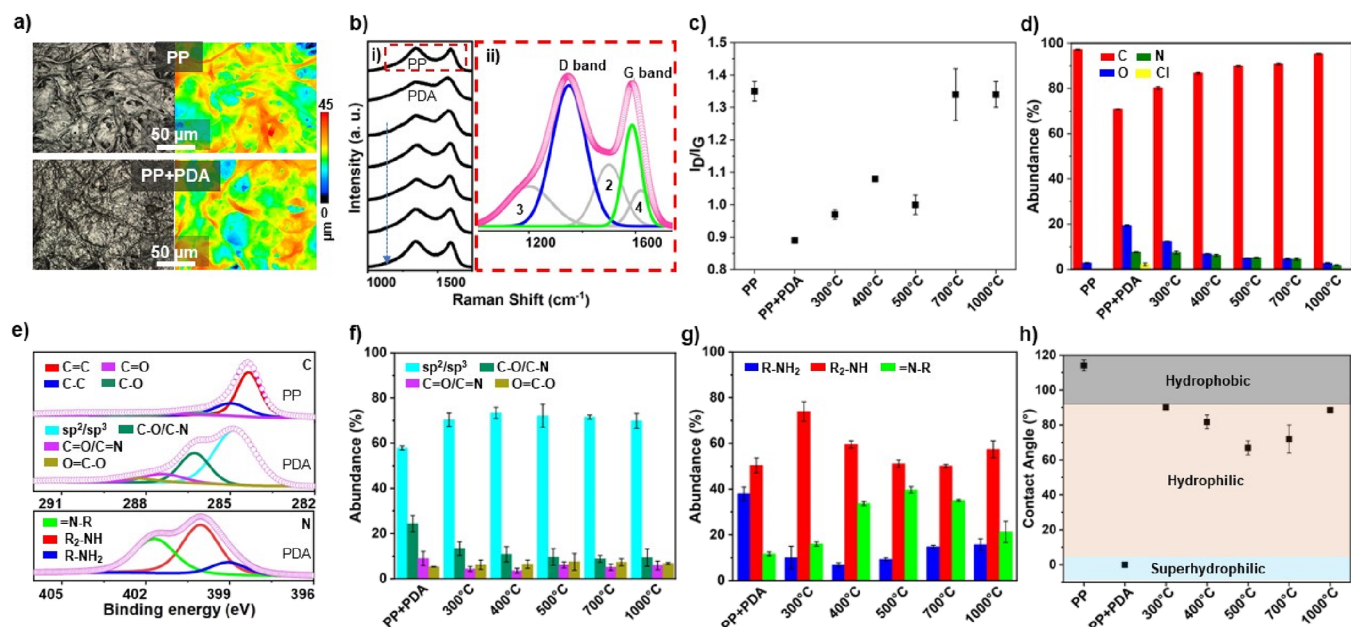
Figure 2. (a) LSCM images of PP and PP+PDA samples. (b) Raman spectrum and (i) PP, PP+PDA and pyrolyzed PDA samples at different temperatures. The blue arrow indicates the temperature increase from top to bottom. (ii) Deconvoluted spectrum. (c) Relation of the degree of structural disorder in carbon samples in PP, PP + PDA, and pyrolyzed PDA at different temperatures. (d) Relative chemical abundance of the atoms on each surface. (e) High-resolution XPS spectra in the C 1s for PP and PP + PDA sample and N 1s region for PDA. (f) Relative chemical abundance of the different carbon species on PP + PDA and thermally treated PDA. (g) Relative chemical abundance of the different nitrogen species on PP + PDA and thermally treated PDA. (h) Contact angle of PP, PP + PDA, and thermally treated PDA. Figure S5 highlights the region of low chemical abundance of panels (d) and (f) for a better visualization.

122-MT-30 diamond knife under room conditions in an RMC Boeckeler PowerTome XL ultramicrotome, resulting in a thin slice. The structural and morphology analyses of isolated PDA before and after heating process were analyzed by TEM images, selected area electron diffraction (SAED), and electron pair distribution function (ePDF). The samples for these analyses were prepared by dropping small pieces of PDA onto a TEM grid used for Cyro EM with holes of 1 μm, and the EDs were taken on the holes.

2.4. Electrical Characterization of PP + PDA Samples

The electrical characteristics of PP samples containing PDA were evaluated by different methods, namely, four-probe sheet resistance (R_s), current−voltage ($I−V$), and Hall effect measurements. The measurements were carried out in a four-probe configuration to minimize the contribution of contact resistance, which may represent ca. 20% of the overall sample resistance. The four-probe R_s measurements were carried out using an Ossila four-point collinear probe system as a function of the temperature of the sample pyrolysis. $I−V$ curves were recorded as a function of the temperature (T) using a Keithley 4200 SCS coupled with an LTS420E Linkam cryogenic probe station. The sample temperature varied from 78 to 303 K, using a 15 K min^{-1} ramp, and held for 3 min at each temperature for signal recording. For the $I−V(T)$ and Hall effect measurements, the electrical connections were established by employing Ag ink and Al (or Au) wires on each edge side of the PP strips. For the Hall effect measurements, the samples were connected on each vertex of the PP squares (size of 1 mm^2). The charge carrier density (n) and mobility (μ) in PP samples were evaluated using a Physical Property Measurement System (PPMS) DynaCoolTM from Quantum Design. Both the longitudinal (R_{xx}) and Hall resistances (R_{xy}) were measured at 30 K in the presence of a perpendicular magnetic field (B) varying from −3 to 3T. The n and μ values were calculated from the angular coefficient (a) of R_{xy} as a function of B, whereas $a = V_H/IB$, where V_H is the Hall voltage and I is the current, and using the sample dimensions, viz., width (W), length (L), and thickness (t). Here, Hall effect measurements were performed to evaluate the impact of PDA addition on the electronic properties of the PP samples. The application of an external magnetic field perpendicular to the current

flow in the sample generates a transverse Hall voltage that allows the calculation of the carrier concentration and mobility.

3. RESULTS AND DISCUSSION

Figure 1a displays a scheme on the functionalization process of PP using PDA. First, we thermally treated cellulose sheets at 1000 °C to convert the entire paper into a conductive material. Such a condition has been explored for the fabrication of many electrochemical devices due to the high conductivity and porosity of the resulting pyrolyzed cellulose sheet.[28−30] The inset SEM image in Figure 1a(i) illustrates the presence of intertwined pyrolyzed fibers and pores. The pyrolysis process decreases the diameter of the fibers, but the material remains porous. The porous structure of PP is a key factor to fabricate 3D electrochemical devices.[44] Next, the PP sheets were immersed in a solution containing dopamine for PDA deposition, as shown in Figure 1a(ii). In such conditions, dopamine autoxidizes in the presence of dissolved oxygen and generates biocompatible films.[32,34] The PDA film deposited onto PP can be visualized in Figure 1a(iii). In this SEM image, it is possible to observe that PDA is molded by the roughness of the fibrous surface, forming a continuous coating that occupies the regions between pores. Finally, in order to tune the chemical composition of PP−PDA interface, we treated the functionalized material at different temperatures as shown in Figure 1a(iv). Our hypothesis is that it is possible to tune the chemical composition and the area of the electrodes due to the thermal treatment, thus demonstrating a new method that allows capillary through of aqueous solutions into the porous and hydrophobic PP.

The morphological changes that occur after each thermal treatment step can be viewed in Figure 1b(i-vi). At 300−400 °C, the morphology of a fibrous material starts to become evident, indicating a reduction in film thickness. The thickness

measurements will be shown ahead. As the temperature increases, it is possible to notice the presence of a fibrous morphology similar to the surface of the PP. In addition, we performed *in situ* SEM imaging while heating PDA-coated sample up to 1000 °C. Video S1 clearly shows the thickness of the film being reduced as the temperature increases. In addition, the formation of microcracks on the PDA film can be observed. To confirm the presence of PDA on thermally heated materials, energy-dispersive X-ray spectroscopy (EDX) measurements were performed, as shown in Figure 1c. By tracking the presence of nitrogen on the surface, it was possible to follow the functionalization process since this chemical element is not present on cellulose. Nitrogen was detected at all temperatures, thus confirming the functionalization process in all conditions investigated. To gain more information about the mass loss occurring during pyrolysis, Figure 1d shows the thermogravimetric analysis of paper, PP, and PDA-modified samples. In the PP sample, a mass loss of approximately 10% up to 185 °C was observed that was attributed to the loss of adsorbed water and degradation of lignocellulosic that did not decompose after pyrolysis.[49] For PDA samples, after an initial mass loss of up to 100 °C due to the presence of adsorbed water molecules, a significant drop was observed at around 250−450 °C due to the pyrolysis-induced building of blocks from PDA.[50,51] Thus, the morphologic changes observed in SEM images at 300−400 °C are consistent with the mass loss observed in TGA curves. The TGA of bare paper was also inserted for comparison.

The roughness of the electrodes was investigated by using LSCM after each heat treatment. The color maps illustrated in Figure 2a clearly illustrated the height variation of PP and PDA-functionalized electrode. The mean roughness of all conditions is around 5.6 ± 0.9 μm due to the roughness of PP, as shown in Figure S4. Thus, the changes observed in the morphology in Figure 1b for each treatment step barely affect the roughness of the electrodes. To study alterations in the carbonaceous structure, we monitored D, D2, D3, D4, and G bands in Raman spectra[29,52] for the thermally treated samples, shown in Figure 2b. The D band ($\sim$1335 cm^{-1}) is related to aromatic clusters with more than six (6) rings, while the D2 ($\sim$1500 cm^{-1}), D3 ($\sim$1200 cm^{-1}), and D4 ($\sim$1620 cm^{-1}) bands are attributed, respectively, to disordered graphene surface layers, functional groups, and small aromatic clusters and ethers. The G band ($\sim$1580 cm^{-1}) is attributed to the in-plane vibration of the sp^2 graphitic structure. The Raman spectrum of the control sample (PP) shows D and G bands located at 1336 and 1594 cm^{-1}, respectively, suggesting presence of disordered carbon and graphitic structures. The broad D band reveals incomplete removal of oxygen from cellulose after pyrolysis.

After PDA functionalization, we observed a slight narrowing of the G band at high temperatures that indicates an improvement of the carbonization process. In addition, the structural disorder was estimated by I_D/I_G ratio, as illustrated in Figure 2c. The D2, D3, and D4 bands were fitted under all conditions investigated to obtain the I_D/I_G ratio. As the temperature increases, higher I_D/I_G ratios were observed. Our results are in agreement with studies reported by Messersmith et al. that obtained a higher I_D/I_G ratio for laser treated PDA onto substrates with increased laser fluence.[53] This result may be related to the lower size of graphitic domains that were reported to have higher I_D/I_G ratios.[54]

By variation of the temperature of pyrolysis, it is also possible to tune the chemical composition of the interface. Figure 2d displays the relative abundance of the species obtained at each temperature by XPS. It is possible to note the predominance of carbon in all samples. For the control sample, i.e., PP, the amount of oxygen observed was lower than 5%, indicating that most of the oxygen content was removed during the heat treatment. For example, the glucose molecule, which is the monomer of cellulose, has a theoretical C/O ratio equal to 1, while PP presented an experimental C/O ratio of approximately 40, thus confirming the significant oxygen removal in the sample. After the modification with PDA, it is possible to verify the insertion of N and O atoms that are present in the dopamine molecule ($C_8H_{11}NO_2$). The presence of Cl in the PDA film is due to the salt form of dopamine (3-hydroxytyramine hydrochloride) employed in this study. By increasing the temperature, a decrease in the percentage of nitrogen on the interface was observed. Thus, to understand the chemical environment of the interface, we next present high-resolution XPS spectra for carbon and nitrogen.

Figure 2e presents the high-resolution XPS spectra in the C 1s and N 1s regions for PP and PP + PDA samples, respectively. For the control sample (PP), it is observed that approximately 50% of the carbon is in sp^2 hybridization ($\sim$284.3 eV). This result is indicative of the formation of π bonds that give rise to the high conductivity of PP.[29] In addition, the presence of carbon with sp^3-type hybridization ($\sim$285.0 eV) was verified, referring to defect-like carbon. The C−O and C=O bonds ($\sim$286.3 and $\sim$288.3 eV, respectively) and the satellite peak π π* ($\sim$290.6 eV) complete the composition of carbon. The observed satellite peak π π* is a characteristic of conjugated systems.[55] After functionalization, in addition to sp^2 and sp^3 carbon, C−N and C=C−O at $\sim$286.3 and $\sim$288.3 eV were observed, respectively, indicating the presence of PDA groups on the surface. In the case of nitrogen species, the PP sample did not show N in its composition, as expected. The high-resolution spectra in the N 1s peak reveal that the N atoms are composed of R−NH$_2$, R$_2$−NH and =N−R (401.1, 400.0, and 398.6 eV, respectively) as shown in Figure 2e. The primary amine is derived from dopamine,[50] while the secondary amine is derived from the intramolecular cyclization products of dopamine to 5,6-indolquinone and 5,6-dihydroxyindole.[56,57] Imines are also formed in the process of dopamine oxidation, as products for the formation of 5,6-dihydroxyindole.[57] Furthermore, the quinone formed is susceptible to reacting with amines via Schiff base reaction, forming imine groups.[58]

The main composition of the interface after each thermal treatment can be observed in Figure 2f,g. While the abundance of sp^2 and sp^3 carbon remains high, it was noted that C−O and C−N decrease as the temperature of pyrolysis increases, as shown in Figure 2f. The amount of nitrogen decreases. However, it is possible to tune the chemical environment of the N species. For instance, freshly deposited PDA has the largest amount of primary amines among the other temperatures investigated. As the temperature increases, the relative abundance of R−NH$_2$ is kept around 8−15% on the interface. Most primary amine groups decay at 300 °C and this result may be attributed to the presence of a significant amount of monomeric (dopamine) and noncyclized oligomeric species that undergo new polymerization due to dehydration, leading to reorientations of structures.[50] One of the key aspects of the

thermal treatment is the possibility of tuning the $R_2-NH/=N-RH$ ratio at the interface.

As demonstrated in the XPS results above, there is a significant change in the chemical composition of nitrogen and oxygenated species that can alter the wettability of the samples. Thus, contact angle measurements were performed to assess the impact of the functionalization on the PP, as shown in Figure 2h. First, the PP sample is hydrophobic since its major chemical composition is composed of sp^2 and sp^3 carbon. The functionalization with PDA promoted an ultralarge drop in the contact angle, from hydrophobic (>90°) to superhydrophilic (<15°). The remarkable increase of C−O and C−N groups when compared to PP is responsible for this change. Videos S2−3 show the hydrophobic and superhydrophilic surfaces. From 300−1000 °C, the contact angles are in the hydrophilic/hydrophobic region. Thus, the functionalization has an enormous impact on the wettability of the interface, changing from hydrophobic to superhydrophilic after PDA introduction and then superhydrophilic to less than 1% away from the cutoff hydrophilic/hydrophobic region with the increase of temperature up to 1000 °C.

We also evaluated the electrical characteristics of the samples. Figure 3a shows the room-temperature R_s values of PP strips as a function of the pyrolysis temperature (T_p). The R_s of PP containing PDA pyrolyzed at 1000 °C is also indicated (PP + PDA). We observe the logarithmic values of R_s

Figure 3. (a) Room-temperature R_s of PP samples as a function of the T_p. The curve fitting corresponds to the equation $\ln(R_s) = 1.3 \times 10^4 e^{-0.015 T_p} + 2.1$. The sample containing PDA pyrolyzed at 1000 °C is also indicated. Inset: Four-point probe setup. The standard deviations of the means R_s are smaller than those of the markers. (b) $I-V$ curves as a function of the sample temperature (T) for PP+PDA pyrolyzed at 1000 °C. (c) Arrhenius plot ($\ln I$ vs $1000/T$) of a representative PP + PDA sample (T_p = 1000 °C) and respective E_a values. The data were obtained from the $I-V(T)$ curves in panel (b). The average E_a for a set of two PP + PDA samples are E_{a1} = 6.6 ± 4.6 meV, E_{a2} = 2.2 ± 0.86 meV, and E_{a3}= 0.9 ± 0.3 meV. (d) Simplified band diagram of PP samples. Ext, Loc, and Def are, respectively, the extended states (red), localized states (green), and defect states (blue) in the sample.

decay exponentially as T_p increases. Higher T_p increases the electrical conduction by boosting the carbon sp^2/sp^3 ratio[29] and/or the percolation between the nanosized sp^2 clusters in the paper matrix, with the delocalization of π electrons being ultimately favored. Here, no significant differences in R_s have been found between nonmodified and PDA-functionalized PP (both pyrolyzed at 1000 °C). We found R_s = 8.6 (±0.3) and 7.2 (±0.6) Ω Sq^{1-} for neat PP and PP + PDA samples. Such a small reduction in R_s suggests that PDA contributes little to the electrical conductivity of the matrix, likely by acting as an additional source of sp^2 carbon moieties that increase electron delocalization.

To gain further insight into the electrical properties of the PP sample, we evaluated their temperature-dependent $I-V$ characteristics. Figure 3b shows the $I-V$ curves of PP+PDA (1000 °C) for temperatures ranging from 78 to 303 K. PP samples absent of PDA and pyrolyzed at different T_p values were also evaluated, as shown in Figure S6. All samples exhibited linear $I-V$ curves where the sample resistance decreases as the temperature increases, indicating a semiconducting behavior. Due to the high current signals registered for the samples pyrolyzed at 1000 °C (both neat PP and PP + PDA), here we limited the current values to 100 mA to avoid Joule heating effects.

The sample $I-V(T)$ response can be expressed using a simple Arrhenius relationship $I = I_0 e^{-Ea/k_BT}$, where k_B is the Boltzmann constant, I_0 is the pre-exponential factor, T is the absolute temperature, and E_a is the charge transport activation energy. Figure 3c depicts the $\ln I$ vs $1000/T$ Arrhenius plot for PP + PDA samples at +0.5 V. Three temperature regimes, namely, 303−183, 163−133, and 123−78 K, have been identified. Similar temperature regions have been observed for PP samples absent of PDA and pyrolyzed at different T_p. Each region in the Arrhenius plot of all samples was fitted by a linear regression exhibiting a coefficient of determination (R^2) > 0.98. The respective E_a values were determined from the curve slope for the three regimes, resulting in values within the meV range and $E_{a1} > E_{a2} > E_{a3}$ for all samples, as shown in Figure S7.

The three E_a values found for all PP samples decay exponentially as T_p increases, following a trend similar to that of $\log R_s$, as shown in Figure S8 and Figure 3a, respectively. Three temperature regimes characterized by $E_{a1} > E_{a2} > E_{a3}$ in the meV range and associated with charge transport governed by extended, localized, and defect states, respectively, have also been observed for other carbon-based semiconductors.[59] At high temperatures carriers are excited into delocalized or extended states (E_{a1}), at intermediate temperatures carriers access localized states (E_{a2}), and at low temperatures conduction occurs via defect states close to the Fermi level (E_F) with energy E_{a3}. The respective regimes are depicted by the red, green, and blue lines in Figure 3c and in the illustrative band diagram in Figure 3d.

In the presence of PDA, we found that E_{a1}, E_{a2}, and E_{a3} reduced by 20−30% in comparison with the activation energies found for the nonmodified PP obtained at 1000 °C. Hall effect measurements show that holes are the majority carriers. We found μ = 0.4 ± 0.1 cm^2 V s^{-1} and n = 4.3 ± 0.5 × 10^{26} m^{-3} for neat PP and μ = 0.6 ± 0.2 cm^2 V s^{-1} and n = 4.4 ± 0.5 × 10^{26} m^{-3} for PP + PDA, as shown in Figure S9, suggesting that no doping occurs in the PP matrix upon PDA addition. Instead, the addition of PDA contributes to the conductivity of the PP matrix mainly as a supplier of energy states for charge
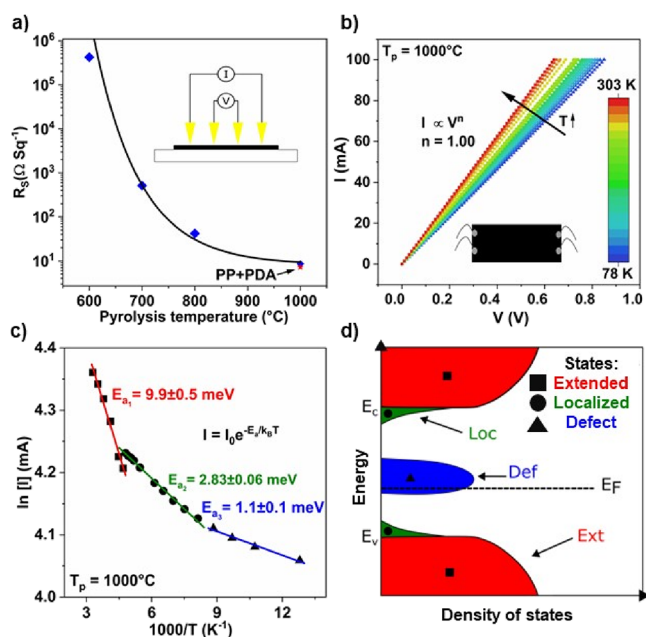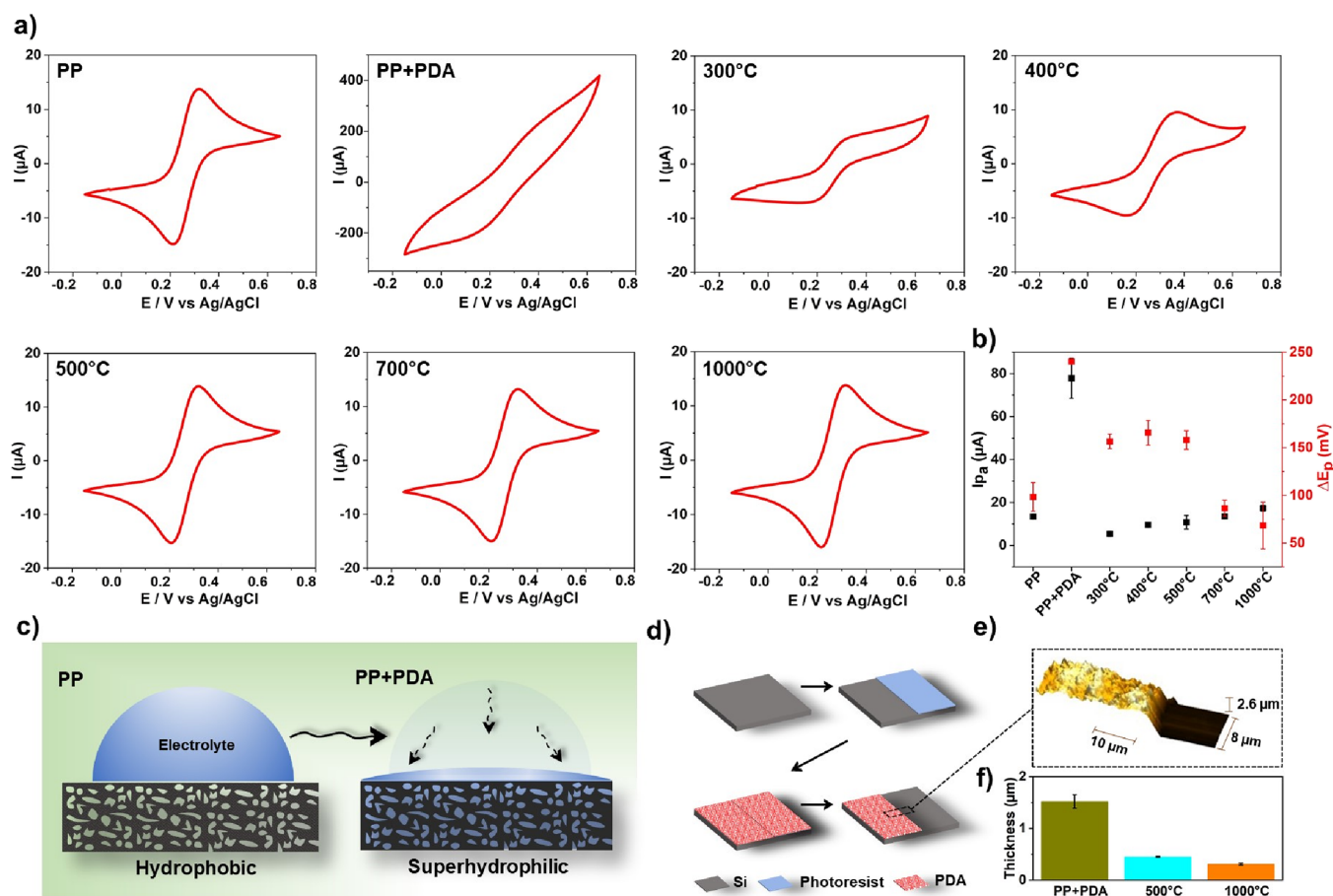
Figure 4. (a) Cyclic voltammograms ($n = 3$) obtained for PP, PP + PDA, and thermally treated PDA at different temperatures (300−1000 °C) in the presence of 5 mM $[Fe(CN)_6]^{3-/4-}$ as a redox probe. Note that PDA remarkably increases the current. (b) Variation of I_p and ΔE_p as a function of the T_p. (c) Schematic illustration of the cross-sectional view of the electrodes for hydrophobicity of PP and PP + PDA. (d) Scheme of the experimental steps to prepare the PDA on a substrate with low roughness. (e) Area measured at the interface Si and Si + PDA. (f) Thickness of the PDA as a function of the temperature ($n = 3$).

transport, likely as an additional source of sp^2 that increases the level of electron delocalization. In other words, PDA acts more like a surface modifier than a dopant or an additional phase in the PP matrix. It is worth emphasizing that Hall measurements performed in porous materials may be subjected to variations of the normal component of the magnetic field due to the nonuniform conducting surfaces within the sample. This can lead to carrier mobilities 10−50 times lower than that of nonporous materials[60] and consequently to higher carrier concentrations. Here, Hall effect measurements were performed to evaluate the effect of PDA addition on the electronic properties of the PP samples, which revealed no doping effects.

We employed cyclic voltammetry to investigate the influence of PDA functionalization on the electrochemical measurements of the electrodes, as shown in Figure 4a. The PP electrode showed a well-defined shape with a peak-to-peak separation (ΔE_p) around 100 mV measured in the presence of a $[Fe(CN)_6]^{3-/4-}$ redox probe. After PDA functionalization, two main changes can be observed: (i) a large current increase and (ii) high ΔE_p values, as shown in Figure 4a. By systematically increasing the temperature from 300 to 1000 °C one can note that ΔE_p decreases, and peak current (I_p) values increase, but they are lower when compared to PDA. We also performed cyclic voltammograms using $[Ru(NH_3)_6]Cl_3$ as a redox probe, as shown in Figure S10. Figure 4b summarizes the variation of I_p and ΔE_p as functions

of the temperature. The results can be explained in the following way. The large current observed after PDA modification, e.g., ∼10× higher, is due to the hydrophilicity of the interface promoted by the addition of N and O groups. As demonstrated in contact angle measurements, the electrolyte penetrates into the bulk region of PP promoting an increase of the area of the electrodes that ultimately results in the large currents obtained.[44,47,48] However, since PDA is not conductive, the ΔE_p values are high in such conditions. Figure 4c shows a schematic illustration of the cross-sectional view of the electrodes. Since PP is hydrophobic the electrolyte is confined at the top face of the electrode. The addition of PDA promotes the capillary flow of the electrolyte into the bulk structure of the paper and consequently increases the area of the electrodes, as shown in Figure 4c.

The fundamental process that allows the electrolyte to advance into the bulk of PDA-coated electrodes can be described by the classical Lucas−Washburn equation (eq 1), which has been used to describe the fluid flows in paper substrates,[61]

$$L(t) = \sqrt{\frac{\gamma \cos\theta r}{2\mu}t}$$

(1)

where L is the penetration length of the fluid front in the material, γ is the fluid surface tension, $\cos\theta$ is the liquid−fiber

contact angle, r is the effective pore radii of the paper, μ is the fluid dynamic viscosity, and t is the time. The pristine PDA coating remarkably reduces the contact angle between the fibers and the electrolyte, thus contributing to the increase in L as predicted in eq 1.

A systematic increase of the temperature improves the electrochemical process, e.g., ΔE_p is lower, occurring at the interface due to the reduction of PDA thickness. Figure 4d shows a scheme of the experimental steps to prepare the PDA on a substrate with low roughness. PDA was deposited on Si substrates using the same experimental conditions employed on PP to allow one to measure the variation of thickness as a function of the temperature. Figure 4e shows the area measured at the interface of Si and Si + PDA. The same process was used to obtain the thickness as a function of the temperature, as demonstrated in Figure 4f. The thickness decreases from approximately 1.5 μm to 350 nm. The thickness of PDA is not uniform over the entire area and some thicker regions also occur on the surface.[28]

TEM techniques were performed to obtain the thickness, morphology, compositional, and structural information on PDA on the top of PP. EELS analyzes reveal and confirm the interface between PP and PDA observed in the HAADF image, Figure 5. As expected, it is difficult to distinguish the interface
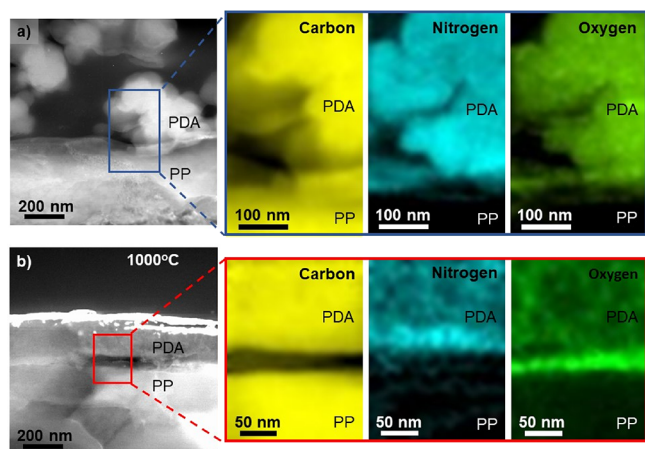

Figure 5. (a) HAADF image with the EELS analysis region marked by a blue rectangular box. (b) HAADF image with the EELS analysis region marked by a red rectangular box. Carbon, nitrogen, and oxygen maps are displayed for the PP + PDA pristine sample and at 1000 °C.

based on the carbon signal since both PP and PDA contain this chemical element. However, we can clearly distinguish the interface based on the nitrogen and oxygen signals. Both signals are higher in the PDA layer than in the PP layer. Thus, our analysis reveals that the PDA layer is formed by mesoparticles with an average size of 150 nm and large pores between them. The large pores observed in the image combined with the surface chemistry of PDA explain the superhydrophilic properties of the electrodes. Figures S11a-b show the image of PP and PP + PDA where the thickness of PDA is about 1.5 μm (we measured the thickness of the PDA layer at different positions).

Additionally, EELS analyses reveal and confirm the interface between PP and PDA observed in the HAADF image after the heating process at 1000 °C; Figure 5. A similar analysis to the previous one can be performed for carbon, nitrogen, and oxygen maps, which means that we cannot distinguish the

interface based on the carbon signal, but we can clearly distinguish the interface based on the nitrogen and oxygen signals. Moreover, the nitrogen and oxygen signals are higher in the thin region analyzed (dark contrast in the HAADF image) and these can be associated with an enrichment of nitrogen and oxygen contents at the PDA and PP surfaces after the heating process, respectively. Thus, it is possible to observe that the PDA layer after the heating process at 1000 °C is almost continuous and has a thickness of approximately 250 nm; see also Figures S11c-d. The reduction observed in the PDA thickness is in agreement with AFM measurement after the heating process. The average spectrum summed in the PDA regions before and after the heating process shows a loss of nitrogen and oxygen in the PDA, and we also observed these losses in the measurements of PDA isolated shown in Figure S12. This result is in agreement with XPS measurements shown in Figure 2f.

Another interesting result obtained by the TEM analyses is related to the degree of ordering of the PDA after the heating process. Figure S12a shows a TEM image of PDA with irregular contours, the corresponding electron diffraction (ED) of the PDA can be seen in Figure S12b, and the ED image is an average of images taken at different PDA positions and corresponds to an amorphous material, which shows large and few peaks in ED. The peaks extracted from ED can be seen in Figure S12c in the inserted graph and their respective distances are 3.65 Å (2.74 nm^{-1}), 2.02 Å (4.95 nm^{-1}), and 1.17 Å (8.56 nm^{-1}) and these distances correspond to amorphous carbon.[62,63] Figure S12c shows the graph corresponding to the electron pair distribution function (ePDF) of the PDA and the distances measured again correspond to amorphous carbon,[64] 1.37, 2.54, 3.79, and 4.91 Å.

The same analysis was performed for the PDA after the heating process at 1000 °C. The TEM image in Figure S12d shows the PDA with facets and lamellar types (inset images show these details). The corresponding ED (Figure S12e) shows a polycrystalline material with a higher order than pristine PDA. The peak distances extracted from the ED (graph inserted in Figure S12f) are 2.10 Å (4.77 nm^{-1}), 1.22 Å (8.23 nm^{-1}), and 1.17 Å (8.54 nm^{-1}), and from the ePDF analysis, they are 1.42, 2.57, 3.89, 5.00, and 6.45 Å (main graph in Figure S12f). These distances correspond to a graphitization of PDA.[65−67] The increase in the degree of ordering (graphitization) was also calculated using the equation for structural length coherence (LSC),[68] which shows an increase from 3.08 Å (PDA) to 6.46 Å (PDA heated to 1000 °C). The LSC can be understood as a volumetric measurement, which means that the graphitization increases approximately 9 times after heating process. Such results help to explain the increase in the conductivity after the heating process.

Finally, as a proof of concept, we explored the surface chemistry of the interface of the electrodes to tune the preparation of AuNPs on the surface of the electrodes. AuNPs are well-known materials to be used in the preparation of electrochemical sensors and biosensors. For example, peptide,[69] aptamers,[70] enzymes,[71] and antibodies[72] have been adsorbed onto gold surfaces to improve the sensitivity of electrochemical biosensors. Here, we explored the surface chemistry of PDA to adsorb [AuCl$_4$]$^−$ ions in the first step and electrochemically reduce them in the second step, as schematically shown in Figure 6a. In addition, it is expected that the large difference in wettability and quantity of N-derived groups can tune some properties in AuNP formation.
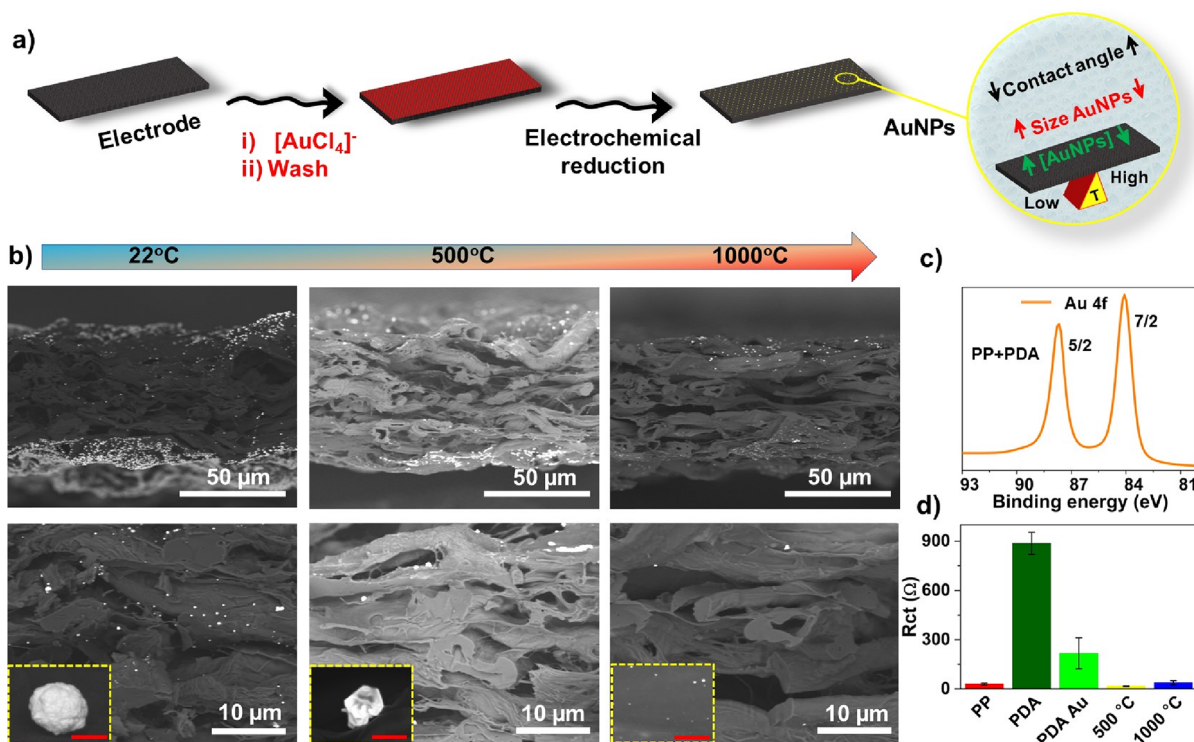
Figure 6. (a) Schematic illustration of the AuNP formation on the electrodes. (b) Cross-sectional SEM images for PDA treated at different temperatures at low magnification (first row) and high magnification (second row). The scale bars in red are 500 nm. (c) XPS spectra for the Au 4f peak of AuNPs synthesized with $[AuCl_4]^-$ on the electrode modified with PDA. (d) R_{ct} in different samples modified with AuNPs.

The pK_a of the protonated amino groups of dopamine is ~10.0 and to make sure that such groups remain protonated during the adsorption and electrochemical reduction, the pH of the solutions was kept below the pK_a of dopamine.[73] After electrochemical reduction, it is possible to observe the presence of AuNPs on the electrodes, white particles in Figure 6b. The top and bottom surfaces of pristine PDA, e.g., 22 °C, contain a large amount of AuNPs that can be explained by the high relative abundance of nitrogen, as confirmed by XPS. In addition, pristine PDA allows aqueous solution to assess inner pores of the electrode, and consequently, AuNPs were also observed in bulk regions of the paper. As the temperature of treated PDA increases, the SEM images show at least three main trends: (i) the amount of AuNPs decreases, (ii) the size of the AuNPs is reduced, and (iii) AuNPs are predominantly formed on the top and bottom face of the PP. The location of the AuNPs (top/bottom face or bulk) is dictated by the wettability of the electrodes. Superhydrophilic electrodes allow nanoparticles to be formed in bulk regions of the paper since the precursors are ions that can diffuse through the pores of the paper before electrochemical reduction. The size of the nanoparticles can be as large as 700 nm in diameter, as the relative abundance of N is higher. We also investigated the AuNP-modified surfaces by using cyclic voltammetry in the presence of a redox probe. Figure S13 shows that I_p and ΔE_p decrease as the temperature increases. These features are particularly important in the development of electrochemical devices for clinical diagnosis, where higher currents with enhanced redox kinetics play an important role.[74] In addition, Figure S14 suggests that mass transport is controlled by diffusion. XPS results confirmed that the amount of gold is higher for PDA and decreases at high temperatures, as shown in Table S1. The high-resolution spectrum for gold illustrated

in Figure 6c indicates a doublet at 84.1 and 87.7 eV that can be attributed to the binding energy of metallic Au ($4f_{7/2}$ and Au(0) $4f_{5/2}$), respectively, thus confirming the electrochemical reduction process. We also observed the same features for all investigated surfaces, as illustrated in Figure S15.

Lastly, we investigated the electrochemical activity of the AuNP-modified electrodes using EIS, as shown in Figure S16. EIS is a remarkable electrochemical technique employed to characterize electrochemical interfaces[29] and biosensors.[69] The R_{ct} was measured by using the modified Randles model to fit the equivalent circuit. Figure 6d shows that Rct values decrease as the temperature of PDA also increases. One of the largest variations in Rct values was observed for PDA kept at 22 °C without the thermal treatment. PDA is not conductive and due to the thickness of the film (~1.5 μm) formed on PP, the largest R_{ct} values were found. However, after the formation of AuNPs on PDA electrodes, a remarkable decrease of R_{ct} was observed. We attributed such a remarkable decrease to the formation of a large amount of AuNPs observed in this experimental condition. In general, the presence of AuNPs enhances the electron transfer rate for the redox probe, which is clearly illustrated in Figure 6. Our results agree with reported works that highlight the positive influence of AuNPs in decreasing R_{ct} on electrodes modified with nonconductive polymers,[75,76] such as PDA.

The electrochemical method reported here brings some advantages compared to traditional AuNP synthesis routes. For instance, our method is simple and fast, it does not require chemical reducing agents to prepare the AuNPs, and the electrochemical reduction can be controlled by selecting a proper reduction potential. In addition, no further purification steps are necessary since the nanoparticles are formed directly on the electrode's surface. For applications that demand a

highly controllable shape, size, and a tunable distance between the AuNPs spots, the bottom up *in situ* growth stands out as remarkable routes.[77] Such routes enable advanced applications using nanopatterned electrodes.[78]

4. CONCLUSIONS

In this work, we report for the first time the pyrolysis of PDA onto PP-based devices to tune surface properties for future applications in diagnostics. The chemical and morphological transformations were followed by several characterization techniques that confirmed superhydrophilic to close to hydrophobic (88.5°) transition and tunable N-based functional groups as the temperature increases. The as-deposited PDA is superhydrophilic, and due to the porous nature of PP, a remarkably large current is observed in the electrochemical experiments. In this case, the R_{ct} is high since PDA has poor electrical properties; however, pyrolyzed PDA shows both low R_{ct} and resistivity, as confirmed by electrical and electrochemical experiments. Current−voltage curves confirm that PDA does not dope the PP matrix but slightly improves the charge transport. TEM revealed the presence of an amorphous film composed of globular nanoparticles containing large pores. After pyrolysis at 1000 °C, PDA was graphitized resulting in a more compact nanofilm adhered on the top of the pyrolyzed fibers.

As-deposited PDA converts the hydrophobic surface of the PP electrode into superhydrophilic, allowing capillary flow of aqueous solutions through the porous material. This new method delivers capillary-through using biocompatible PDA without the need of prior dropping of alcohols[44] or hydrophilic layers[45] underneath the carbon electrode. In addition, since conductivity is important to further improve the performance of electrochemical sensors,[79] the pyrolysis process can promote a graphitization of PDA and tune the chemical composition of the interface. To highlight the interesting properties of PDA, we show the preparation of AuNPs at the interface. The size, concentration, and distribution along the thickness of the paper can be tuned by selecting the proper temperature for the pyrolysis of PDA. In addition, our procedure is less laborious when compared to traditional citrated-capped method to prepare AuNPs.[80] The presence of AuNPs was confirmed by SEM-EDS and XPS experiments. Thus, our work paves the way for the fabrication of paper-based electrochemical biosensors with a tunable electrochemical active area and surface chemistry. In addition, the well-known chemical reactions that use N-based groups, such as (3-dimethylamino-propyl)-ethyl-carbodiimide and *N*-hydroxysuccinimide (EDC/NHS),[81] or gold as a platform to immobilize recognizing species, can be adopted using our route. In addition, since PP is brittle, future work should address this important issue to fabricate miniaturized electrochemical devices.

ASSOCIATED CONTENT

Supporting Information

The Supporting Information is available free of charge at https://pubs.acs.org/doi/10.1021/acsmeasuresciau.3c00063.

> Scheme of the assembly process to fabricate the WE; image of the *in situ* heating stage; scheme of the equipment and materials used to measure the resistivity; LSCM images of samples; experiments as a function of temperature; Arrhenius plot; activation energies as a function of the T_p; Hall coefficient as a function of the magnetic field; TEM images; scan rate study; XPS study (PDF)

> In situ SEM imaging at temperatures from 25 to 1000 °C (MP4)

> Hydrophobic surface (MP4)

> Superhydrophilic surface (MP4)

AUTHOR INFORMATION

Corresponding Author

Murilo Santhiago − *Brazilian Nanotechnology National Laboratory, Brazilian Center for Research in Energy and Materials, Campinas 13083-100, Brazil; Federal University of ABC, Santo André 09210-580, Brazil;* orcid.org/0000-0002-9146-9677; Email: murilo.santhiago@lnnano.cnpem.br

Authors

Jaqueline F. Rocha − *Brazilian Nanotechnology National Laboratory, Brazilian Center for Research in Energy and Materials, Campinas 13083-100, Brazil; Federal University of ABC, Santo André 09210-580, Brazil*

Julia C. de Oliveira − *Brazilian Nanotechnology National Laboratory, Brazilian Center for Research in Energy and Materials, Campinas 13083-100, Brazil*

Jefferson Bettini − *Brazilian Nanotechnology National Laboratory, Brazilian Center for Research in Energy and Materials, Campinas 13083-100, Brazil*

Mathias Strauss − *Brazilian Nanotechnology National Laboratory, Brazilian Center for Research in Energy and Materials, Campinas 13083-100, Brazil*

Guilherme S. Selmi − *Brazilian Nanotechnology National Laboratory, Brazilian Center for Research in Energy and Materials, Campinas 13083-100, Brazil; Universidade Estadual de Campinas, Instituto de Física Gleb Wataghin, Campinas 13083-859, Brazil;* orcid.org/0009-0002-7645-9398

Anderson K. Okazaki − *Brazilian Nanotechnology National Laboratory, Brazilian Center for Research in Energy and Materials, Campinas 13083-100, Brazil;* orcid.org/0000-0003-1935-9841

Rafael F. de Oliveira − *Brazilian Nanotechnology National Laboratory, Brazilian Center for Research in Energy and Materials, Campinas 13083-100, Brazil; Universidade Estadual de Campinas, Instituto de Física Gleb Wataghin, Campinas 13083-859, Brazil*

Renato S. Lima − *Brazilian Nanotechnology National Laboratory, Brazilian Center for Research in Energy and Materials, Campinas 13083-100, Brazil; Federal University of ABC, Santo André 09210-580, Brazil; Institute of Chemistry, University of Campinas, Campinas 13083-970, Brazil; São Carlos Institute of Chemistry, University of São Paulo, São Carlos 09210-580, Brazil;* orcid.org/0000-0001-8450-1475

Complete contact information is available at:
https://pubs.acs.org/10.1021/acsmeasuresciau.3c00063

Author Contributions

J.F.R. and J.C.O. prepared the functionalized PP and performed the electrochemical experiments and characterization studies. J.B. conducted and discussed TEM results. M.Strauss helped with Raman measurements and discussions.

■ ABBREVIATIONS

PDA- polydopamine
PP- pyrolyzed paper
AuNPs- gold nanoparticles

■ REFERENCES

(1) Dungchai, W.; Chailapakul, O.; Henry, C. S. Electrochemical Detection for Paper-Based Microfluidics. *Anal. Chem.* **2009**, *81* (14), 5821−5826.

(2) Nie, Z.; Nijhuis, C. A.; Gong, J.; Chen, X.; Kumachev, A.; Martinez, A. W.; Narovlyansky, M.; Whitesides, G. M. Electrochemical Sensing in Paper-Based Microfluidic Devices. *Lab Chip* **2010**, *10* (4), 477−483.

(3) Clark, K. M.; Schenkel, M. S.; Pittman, T. W.; Samper, I. C.; Anderson, L. B. R.; Khamcharoen, W.; Elmegerhi, S.; Perera, R.; Siangproh, W.; Kennan, A. J.; Geiss, B. J.; Dandy, D. S.; Henry, C. S. Electrochemical Capillary Driven Immunoassay for Detection of SARS-CoV-2. *ACS Meas. Sci. Au* **2022**, *2* (6), 584−594.

(4) Santhiago, M.; da Costa, P. G.; Pereira, M. P.; Corrêa, C. C.; de Morais, V. B.; Bufon, C. C. B. Versatile and Robust Integrated Sensors To Locally Assess Humidity Changes in Fully Enclosed Paper-Based Devices. *ACS Appl. Mater. Interfaces* **2018**, *10* (41), 35631−35638.

(5) Phoonsawat, K.; Agir, I.; Dungchai, W.; Ozer, T.; Henry, C. S. A Smartphone-Assisted Hybrid Sensor for Simultaneous Potentiometric and Distance-Based Detection of Electrolytes. *Anal. Chim. Acta* **2022**, *1226*, No. 340245.

(6) Noviana, E.; McCord, C. P.; Clark, K. M.; Jang, I.; Henry, C. S. Electrochemical Paper-Based Devices: Sensing Approaches and Progress toward Practical Applications. *Lab Chip* **2020**, *20* (1), 9−34.

(7) Xiong, C.; Yang, Q.; Dang, W.; Zhou, Q.; Jiang, X.; Sun, X.; Wang, Z.; An, M.; Ni, Y. A Multifunctional Paper-Based Super-capacitor with Excellent Temperature Adaptability, Plasticity, Tensile Strength, Self-Healing, and High Thermoelectric Effects. *J. Mater. Chem. A* **2023**, *11* (9), 4769−4779.

(8) Yao, B.; Zhang, J.; Kou, T.; Song, Y.; Liu, T.; Li, Y. Paper-Based Electrodes for Flexible Energy Storage Devices. *Advanced Science* **2017**, *4* (7), 1700107.

(9) Juqu, T.; Willenberg, S. C.; Pokpas, K.; Ross, N. Advances in Paper-Based Battery Research for Biodegradable Energy Storage. *Advanced Sensor and Energy Materials* **2022**, *1* (4), No. 100037.

(10) Hamedi, M. M.; Ainla, A.; Güder, F.; Christodouleas, D. C.; Fernández-Abedul, M. T.; Whitesides, G. M. Integrating Electronics and Microfluidics on Paper. *Adv. Mater.* **2016**, *28* (25), 5054−5063.

(11) Santhiago, M.; Bettini, J.; Araújo, S. R.; Bufon, C. C. B. Three-Dimensional Organic Conductive Networks Embedded in Paper for Flexible and Foldable Devices. *ACS Appl. Mater. Interfaces* **2016**, *8* (17), 10661−10664.

(12) Santhiago, M.; Corrêa, C. C.; Bernardes, J. S.; Pereira, M. P.; Oliveira, L. J. M.; Strauss, M.; Bufon, C. C. B. Flexible and Foldable Fully-Printed Carbon Black Conductive Nanostructures on Paper for High-Performance Electronic, Electrochemical, and Wearable Devices. *ACS Appl. Mater. Interfaces* **2017**, *9* (28), 24365−24372.

(13) Pandoli, O. G.; Neto, R. J. G.; Oliveira, N. R.; Fingolo, A. C.; Corrêa, C. C.; Ghavami, K.; Strauss, M.; Santhiago, M. Ultra-Highly Conductive Hollow Channels Guided by a Bamboo Bio-Template for Electric and Electrochemical Devices. *J. Mater. Chem. A* **2020**, *8* (7), 4030−4039.

(14) He, Y.; Lin, X.; Feng, Y.; Luo, B.; Liu, M. Carbon Nanotube Ink Dispersed by Chitin Nanocrystals for Thermoelectric Converter for Self-Powering Multifunctional Wearable Electronics. *Adv. Sci.* **2022**, *9*, 2204675 DOI: 10.1002/advs.202204675.

(15) Liu, M.; Yang, J.; Wang, J.; Liu, Z.; Hu, C. Light-Addressable Paper-Based Photoelectrochemical Analytical Device with Tunable Detection Throughput for On-Site Biosensing. *Anal. Chem.* **2022**, *94* (2), 583−587.

(16) Kudr, J.; Zhao, L.; Nguyen, E. P.; Arola, H.; Nevanen, T. K.; Adam, V.; Zitka, O.; Merkoçi, A. Inkjet-Printed Electrochemically Reduced Graphene Oxide Microelectrode as a Platform for HT-2 Mycotoxin Immunoenzymatic Biosensing. *Biosens. Bioelectron.* **2020**, *156*, No. 112109.

(17) Zhao, L.; Rosati, G.; Piper, A.; de Carvalho Castro e Silva, C.; Hu, L.; Yang, Q.; Della Pelle, F.; Alvarez-Diduk, R. R.; Merkoçi, A. Laser Reduced Graphene Oxide Electrode for Pathogenic Escherichia Coli Detection. *ACS Appl. Mater. Interfaces* **2023**, *15* (7), 9024−9033.

(18) Hasimoto, L. H.; Corrêa, C. C.; Costa, C. A. R.; Santhiago, M. Polydopamine Nanofilms for High-Performance Paper-Based Electrochemical Devices. *Biopolymers* **2021**, *112* (12), No. e23472.

(19) Santhiago, M.; Strauss, M.; Pereira, M. P.; Chagas, A. S.; Bufon, C. C. B. Direct Drawing Method of Graphite onto Paper for High-Performance Flexible Electrochemical Sensors. *ACS Appl. Mater. Interfaces* **2017**, *9* (13), 11959−11966.

(20) Yu, H.; Han, H.; Jang, J.; Cho, S. Fabrication and Optimization of Conductive Paper Based on Screen-Printed Polyaniline/Graphene Patterns for Nerve Agent Detection. *ACS Omega* **2019**, *4* (3), 5586−5594.

(21) Yamada, K.; Henares, T. G.; Suzuki, K.; Citterio, D. Paper-Based Inkjet-Printed Microfluidic Analytical Devices. *Angew. Chem., Int. Ed.* **2015**, *54* (18), 5294−5310.

(22) Yáñez-Sedeño, P.; Campuzano, S.; Pingarrón, J. M. Screen-Printed Electrodes: Promising Paper and Wearable Transducers for (Bio)Sensing. *Biosensors* **2020**, *10* (7), 76.

(23) Kassem, I.; Ablouh, E.-H.; El Bouchtaoui, F.-Z.; Hannache, H.; Ghalfi, H.; Sehaqui, H.; El Achaby, M. Cellulose Nanofibers/Engineered Biochar Hybrid Materials as Biodegradable Coating for Slow-Release Phosphate Fertilizers. *ACS Sustainable Chem. Eng.* **2022**, *10* (46), 15250−15262.

(24) Kane, S.; Ulrich, R.; Harrington, A.; Stadie, N. P.; Ryan, C. Physical and Chemical Mechanisms That Influence the Electrical Conductivity of Lignin-Derived Biochar. *Carbon Trends* **2021**, *5*, No. 100088.

(25) Fingolo, A. C.; Bettini, J.; da Silva Cavalcante, M.; Pereira, M. P.; Bufon, C. C. B.; Santhiago, M.; Strauss, M. Boosting Electrical Conductivity of Sugarcane Cellulose and Lignin Biocarbons through Annealing under Isopropanol Vapor. *ACS Sustainable Chem. Eng.* **2020**, *8* (18), 7002−7010.

(26) Lima, R. S.; Strauss, M.; Santhiago, M.Sensing Materials: Flexible Carbon-Based Electrochemical Devices Based on the Three-Dimensional Architecture of Paper. *Encycl. Sens. Biosens.* 2023, 600 Elsevier DOI: DOI: 10.1016/B978-0-12-822548-6.00026-1.

(27) Ye, R.; James, D. K.; Tour, J. M. Laser-Induced Graphene: From Discovery to Translation. *Adv. Mater.* **2019**, *31* (1), 1803621.

(28) Damasceno, S.; Corrêa, C. C.; Gouveia, R. F.; Strauss, M.; Bufon, C. C. B.; Santhiago, M. Delayed Capillary Flow of Elastomers: An Efficient Method for Fabrication and Nanofunctionalization of Flexible, Foldable, Twistable, and Stretchable Electrodes from Pyrolyzed Paper. *Advanced Electronic Materials* **2020**, *6* (1), 1900826.

(29) Tinoco, M. V. D. L.; Fujii, L. R.; Nicoliche, C. Y. N.; Giordano, G. F.; Barbosa, J. A.; da Rocha, J. F.; dos Santos, G. T.; Bettini, J.; Santhiago, M.; Strauss, M.; Lima, R. S. Scalable and Green Formation of Graphitic Nanolayers Produces Highly Conductive Pyrolyzed Paper toward Sensitive Electrochemical Sensors. *Nanoscale* 2023, *15* (13), 6201−6214.

(30) Nicoliche, C. Y. N.; Pascon, A. M.; Bezerra, Í. R. S.; de Castro, A. C. H.; Martos, G. R.; Bettini, J.; Alves, W. A.; Santhiago, M.; Lima, R. S. In Situ Nanocoating on Porous Pyrolyzed Paper Enables Antibiofouling and Sensitive Electrochemical Analyses in Biological Fluids. *ACS Appl. Mater. Interfaces* **2022**, *14* (2), 2522−2533.

(31) Giuliani, J. G.; Benavidez, T. E.; Duran, G. M.; Vinogradova, E.; Rios, A.; Garcia, C. D. Development and Characterization of Carbon Based Electrodes from Pyrolyzed Paper for Biosensing Applications. *J. Electroanal. Chem.* **2016**, *765*, 8−15.

(32) Lee, H.; Dellatore, S. M.; Miller, W. M.; Messersmith, P. B. Mussel-Inspired Surface Chemistry for Multifunctional Coatings. *Science* **2007**, *318* (5849), 426−430.

(33) Ryu, J. H.; Messersmith, P. B.; Lee, H. Polydopamine Surface Chemistry: A Decade of Discovery. *ACS Appl. Mater. Interfaces* **2018**, *10* (9), 7523−7540.

(34) Rocha, J. F.; Hasimoto, L. H.; Santhiago, M. Recent Progress and Future Perspectives of Polydopamine Nanofilms toward Functional Electrochemical Sensors. *Anal. Bioanal. Chem.* **2023**, *415*, 3799.

(35) Kanitthamniyom, P.; Zhang, Y. Application of Polydopamine in Biomedical Microfluidic Devices. *Microfluid Nanofluid* **2018**, *22* (3), 24.

(36) Palladino, P.; Bettazzi, F.; Scarano, S. Polydopamine: Surface Coating, Molecular Imprinting, and Electrochemistry—Successful Applications and Future Perspectives in (Bio)Analysis. *Anal Bioanal Chem.* **2019**, *411* (19), 4327−4338.

(37) Hou, C.; Zhang, X.; Wang, L.; Zhang, F.; Huang, X.; Wang, Z. A Buckypaper Decorated with CoP/Co for Nonenzymatic Amperometric Sensing of Glucose. *Microchim Acta* **2020**, *187* (2), 101.

(38) Xu, Z.; Han, R.; Liu, N.; Gao, F.; Luo, X. Electrochemical Biosensors for the Detection of Carcinoembryonic Antigen with Low Fouling and High Sensitivity Based on Copolymerized Polydopamine and Zwitterionic Polymer. *Sens. Actuators, B* **2020**, *319*, No. 128253.

(39) Chang, F.; Wang, H.; He, S.; Gu, Y.; Zhu, W.; Li, T.; Ma, R. Simultaneous Determination of Hydroquinone and Catechol by a Reduced Graphene Oxide—Polydopamine—Carboxylated Multi-Walled Carbon Nanotube Nanocomposite. *RSC Adv.* **2021**, *11* (51), 31950−31958.

(40) Zhang, F.; Fan, L.; Liu, Z.; Han, Y.; Guo, Y. A Label-Free Electrochemical Aptasensor for the Detection of Cancer Antigen 125 Based on Nickel Hexacyanoferrate Nanocubes/Polydopamine Functionalized Graphene. *J. Electroanal. Chem.* **2022**, *918*, No. 116424.

(41) Yadav, S.; Sadique, M. A.; Ranjan, P.; Khan, R.; Sathish, N.; Srivastava, A. K. Polydopamine Decorated MoS2 Nanosheet Based Electrochemical Immunosensor for Sensitive Detection of SARS-CoV-2 Nucleocapsid Protein in Clinical Samples. *J. Mater. Chem. B* **2022**, *10* (41), 8478−8489.

(42) Kim, S.; Jang, L. K.; Jang, M.; Lee, S.; Hardy, J. G.; Lee, J. Y. Electrically Conductive Polydopamine−Polypyrrole as High Performance Biomaterials for Cell Stimulation in Vitro and Electrical Signal Recording in Vivo. *ACS Appl. Mater. Interfaces* **2018**, *10* (39), 33032−33042.

(43) Niu, B.; Hua, T.; Xu, B. Robust Deposition of Silver Nanoparticles on Paper Assisted by Polydopamine for Green and Flexible Electrodes. *ACS Sustainable Chem. Eng.* **2020**, *8* (34), 12842−12851.

(44) Shimizu, F. M.; Pasqualeti, A. M.; Nicoliche, C. Y. N.; Gobbi, A. L.; Santhiago, M.; Lima, R. S. Alcohol-Triggered Capillarity through Porous Pyrolyzed Paper-Based Electrodes Enables Ultrasensitive Electrochemical Detection of Phosphate. *ACS Sens.* **2021**, *6* (8), 3125−3132.

(45) Bezinge, L.; Lesinski, J. M.; Suea-Ngam, A.; Richards, D. A.; deMello, A. J.; Shih, C.-J. Paper-Based Laser-Pyrolyzed Electrofluidics: An Electrochemical Platform for Capillary-Driven Diagnostic Bioassays. *Adv. Mater.* **2023**, *35* (30), 2302893.

(46) Bisht, N.; Dwivedi, N.; Khosla, A.; Mondal, D. P.; Srivastava, A. K.; Dhand, C. Review—Recent Advances in Polydopamine-Based Electrochemical Biosensors. *J. Electrochem. Soc.* **2022**, *169* (10), 107505.

(47) Barbosa, J. A.; Freitas, V. M. S.; Vidotto, L. H. B.; Schleder, G. R.; de Oliveira, R. A. G.; da Rocha, J. F.; Kubota, L. T.; Vieira, L. C. S.; Tolentino, H. C. N.; Neckel, I. T.; Gobbi, A. L.; Santhiago, M.; Lima, R. S. Biocompatible Wearable Electrodes on Leaves toward the On-Site Monitoring of Water Loss from Plants. *ACS Appl. Mater. Interfaces* **2022**, *14* (20), 22989−23001.

(48) Hasimoto, L. H.; Bettini, J.; Leite, E. R.; Lima, R. S.; Souza Junior, J. B.; Liu, L.; Santhiago, M. Binary Cooperative Thermal Treatment of Cellulose and MoS2 for the Preparation of Sustainable Paper-Based Electrochemical Devices for Hydrogen Evolution. *ACS Appl. Eng. Mater.* **2023**, *1* (2), 708−719.

(49) Yao, Y.; Gao, B.; Chen, J.; Yang, L. Engineered Biochar Reclaiming Phosphate from Aqueous Solutions: Mechanisms and Potential Application as a Slow-Release Fertilizer. *Environ. Sci. Technol.* **2013**, *47* (15), 8700−8708.

(50) Malollari, K. G.; Delparastan, P.; Sobek, C.; Vachhani, S. J.; Fink, T. D.; Zha, R. H.; Messersmith, P. B. Mechanical Enhancement of Bioinspired Polydopamine Nanocoatings. *ACS Appl. Mater. Interfaces* **2019**, *11* (46), 43599−43607.

(51) Li, Y.; Luo, L.; Nie, M.; Davenport, A.; Li, Y.; Li, B.; Choy, K.-L. A Graphene Nanoplatelet-Polydopamine Molecularly Imprinted Biosensor for Ultratrace Creatinine Detection. *Biosens. Bioelectron.* **2022**, *216*, No. 114638.

(52) Maliutina, K.; Tahmasebi, A.; Yu, J. Effects of Pressure on Morphology and Structure of Bio-Char from Pressurized Entrained-Flow Pyrolysis of Microalgae. *Data in Brief* **2018**, *18*, 422−431.

(53) Lee, K.; Park, M.; Malollari, K. G.; Shin, J.; Winkler, S. M.; Zheng, Y.; Park, J. H.; Grigoropoulos, C. P.; Messersmith, P. B. Laser-Induced Graphitization of Polydopamine Leads to Enhanced Mechanical Performance While Preserving Multifunctionality. *Nat. Commun.* **2020**, *11* (1), 4848.

(54) Sato, K.; Saito, R.; Oyama, Y.; Jiang, J.; Cançado, L. G.; Pimenta, M. A.; Jorio, A.; Samsonidze, Ge. G.; Dresselhaus, G.; Dresselhaus, M. S. D-Band Raman Intensity of Graphitic Materials as a Function of Laser Energy and Crystallite Size. *Chem. Phys. Lett.* **2006**, *427* (1), 117−121.

(55) Tang, M.-C.; Zhang, S.; Magnanelli, T. J.; Nguyen, N. V.; Heilweil, E. J.; Anthopoulos, T. D.; Hacker, C. A. Unraveling the Compositional Heterogeneity and Carrier Dynamics of Alkali Cation Doped 3D/2D Perovskites with Improved Stability. *Mater. Adv.* **2021**, *2* (4), 1253−1262.

(56) Qu, K.; Wang, Y.; Vasileff, A.; Jiao, Y.; Chen, H.; Zheng, Y. Polydopamine-Inspired Nanomaterials for Energy Conversion and Storage. *J. Mater. Chem. A* **2018**, *6* (44), 21827−21846.

(57) Zangmeister, R. A.; Morris, T. A.; Tarlov, M. J. Characterization of Polydopamine Thin Films Deposited at Short Times by Autoxidation of Dopamine. *Langmuir* **2013**, *29* (27), 8619−8628.

(58) Chen, S.; Cao, Y.; Feng, J. Polydopamine As an Efficient and Robust Platform to Functionalize Carbon Fiber for High-Performance Polymer Composites. *ACS Appl. Mater. Interfaces* **2014**, *6* (1), 349−356.

(59) Zhai, Z.; Shen, H.; Chen, J.; Li, X.; Jiang, Y. Evolution of Structural and Electrical Properties of Carbon Films from Amorphous Carbon to Nanocrystalline Graphene on Quartz Glass by HFCVD. *ACS Appl. Mater. Interfaces* **2018**, *10* (20), 17427−17436.

(60) Ito, Y.; Tanabe, Y.; Sugawara, K.; Koshino, M.; Takahashi, T.; Tanigaki, K.; Aoki, H.; Chen, M. Three-Dimensional Porous Graphene Networks Expand Graphene-Based Electronic Device Applications. *Phys. Chem. Chem. Phys.* **2018**, *20* (9), 6024−6033.

(61) Gong, M. M.; Sinton, D. Turning the Page: Advancing Paper-Based Microfluidics for Broad Diagnostic Application. *Chem. Rev.* **2017**, *117* (12), 8447−8480.

(62) Schultrich, B. Structure of Amorphous Carbon. In *Tetrahedrally Bonded Amorphous Carbon Films I: Basics, Structure and Preparation*; Schultrich, B., Ed.; Springer Series in Materials Science; Springer: Berlin, Heidelberg, 2018; pp 195−272. DOI: 10.1007/978-3-662-55927-7_6.

(63) Bhattarai, B.; Pandey, A.; Drabold, D. A. Evolution of Amorphous Carbon across Densities: An Inferential Study. *Carbon* **2018**, *131*, 168−174.

(64) Wang, C.-Z.; Lee, G.-D.; Li, J.; Yip, S.; Ho, K.-M. Atomistic Simulation Studies of Complex Carbon and Silicon Systems Using Environment-Dependent Tight-Binding Potentials. In *Scientific Modeling and Simulations*; Yip, S., de la Rubia, T. D., Eds.; Lecture Notes in Computational Science and Engineering; Springer: Netherlands, 2009; pp 97−121. DOI: 10.1007/978-1-4020-9741-6_9.

(65) Maia, F. C. B.; Samad, R. E.; Bettini, J.; Freitas, R. O.; Vieira Junior, N. D.; Souza-Neto, N. M. Synthesis of Diamond-like Phase from Graphite by Ultrafast Laser Driven Dynamical Compression. *Sci. Rep* **2015**, *5* (1), 11812.

(66) de Paiva, M. V.; Bettini, J.; Colombari, F. M.; Fazzio, A.; Strauss, M. Unveiling Electrical Anisotropy of Hierarchical Pyrolytic Biocarbons from Wood Cellulose. *J. Mater. Sci.* **2022**, *57* (48), 21980−21995.

(67) Ehi-Eromosele, C. O.; Onwucha, C. N.; Ajayi, S. O.; Melinte, G.; Hansen, A.-L.; Indris, S.; Ehrenberg, H. Ionothermal Synthesis of Activated Carbon from Waste PET Bottles as Anode Materials for Lithium-Ion Batteries. *RSC Adv.* **2022**, *12* (53), 34670−34684.

(68) Schleder, G. R.; Azevedo, G. M.; Nogueira, I. C.; Rebelo, Q. H. F.; Bettini, J.; Fazzio, A.; Leite, E. R. Decreasing Nanocrystal Structural Disorder by Ligand Exchange: An Experimental and Theoretical Analysis. *J. Phys. Chem. Lett.* **2019**, *10* (7), 1471−1476.

(69) Castro, A. C. H.; Bezerra, Í. R. S.; Pascon, A. M.; da Silva, G. H.; Philot, E. A.; de Oliveira, V. L.; Mancini, R. S. N.; Schleder, G. R.; Castro, C. E.; de Carvalho, L. R. S.; Fernandes, B. H. V.; Cilli, E. M.; Sanches, P. R. S.; Santhiago, M.; Charlie-Silva, I.; Martinez, D. S. T.; Scott, A. L.; Alves, W. A.; Lima, R. S. Modular Label-Free Electrochemical Biosensor Loading Nature-Inspired Peptide toward the Widespread Use of COVID-19 Antibody Tests. *ACS Nano* **2022**, *16*, 14239 DOI: 10.1021/acsnano.2c04364.

(70) Xie, Y.; Huang, Y.; Li, J.; Wu, J. A Trigger-Based Aggregation of Aptamer-Functionalized Gold Nanoparticles for Colorimetry: An Example on Detection of Escherichia Coli O157:H7. *Sens. Actuators, B* **2021**, *339*, No. 129865.

(71) Gherardi, F.; Turyanska, L.; Ferrari, E.; Weston, N.; Fay, M. W.; Colston, B. J. Immobilized Enzymes on Gold Nanoparticles: From Enhanced Stability to Cleaning of Heritage Textiles. *ACS Appl. Bio Mater.* **2019**, *2* (11), 5136−5143.

(72) Sadique, M. A.; Yadav, S.; Ranjan, P.; Khan, R.; Khan, F.; Kumar, A.; Biswas, D. Highly Sensitive Electrochemical Immuno-sensor Platforms for Dual Detection of SARS-CoV-2 Antigen and Antibody Based on Gold Nanoparticle Functionalized Graphene Oxide Nanocomposites. *ACS Appl. Bio Mater.* **2022**, *5* (5), 2421−2430.

(73) Hemmatpour, H.; De Luca, O.; Crestani, D.; Stuart, M. C. A.; Lasorsa, A.; van der Wel, P. C. A.; Loos, K.; Giousis, T.; Haddadi-Asl, V.; Rudolf, P. New Insights in Polydopamine Formation via Surface Adsorption. *Nat. Commun.* **2023**, *14* (1), 664.

(74) Liu, G.; Rusling, J. F. COVID-19 Antibody Tests and Their Limitations. *ACS Sens.* **2021**, *6* (3), 593−612.

(75) Linh, N. D.; Huyen, N. T. T.; Dang, N. H.; Piro, B.; Thu, V. T. Electrochemical Interface Based on Polydopamine and Gold Nano-particles/Reduced Graphene Oxide for Impedimetric Detection of Lung Cancer Cells. *RSC Adv.* **2023**, *13* (15), 10082−10089.

(76) Lázaro-Martínez, J. M.; Byrne, A. J.; Rodríguez-Castellón, E.; Manrique, J. M.; Jones, L. R.; Campo Dall' Orto, V. Linear Polyethylenimine-Decorated Gold Nanoparticles: One-Step Electro-deposition and Studies of Interaction with Viral and Animal Proteins. *Electrochim. Acta* **2019**, *301*, 126−135.

(77) Vinnacombe-Willson, G. A.; Conti, Y.; Stefancu, A.; Weiss, P. S.; Cortés, E.; Scarabelli, L. Direct Bottom-Up In Situ Growth: A Paradigm Shift for Studies in Wet-Chemical Synthesis of Gold Nanoparticles. *Chem. Rev.* **2023**, *123* (13), 8488−8529.

(78) Hüttenhofer, L.; Golibrzuch, M.; Bienek, O.; Wendisch, F. J.; Lin, R.; Becherer, M.; Sharp, I. D.; Maier, S. A.; Cortés, E. Metasurface Photoelectrodes for Enhanced Solar Fuel Generation. *Adv. Energy Mater.* **2021**, *11* (46), 2102877.

(79) de Brito Ayres, L.; Brooks, J.; Whitehead, K.; Garcia, C. D. Rapid Detection of Staphylococcus Aureus Using Paper-Derived Electrochemical Biosensors. *Anal. Chem.* **2022**, *94* (48), 16847−16854.

(80) Alafeef, M.; Dighe, K.; Moitra, P.; Pan, D. Rapid, Ultrasensitive, and Quantitative Detection of SARS-CoV-2 Using Antisense Oligonucleotides Directed Electrochemical Biosensor Chip. *ACS Nano* **2020**, *14* (12), 17028−17045.

(81) Hondred, J. A.; Medintz, I. L.; Claussen, J. C. Enhanced Electrochemical Biosensor and Supercapacitor with 3D Porous Architectured Graphene via Salt Impregnated Inkjet Maskless Lithography. *Nanoscale Horizons* **2019**, *4* (3), 735−746.

M